

Real-MFF Dataset: A large and realistic multi-focus image dataset with ground truth

Juncheng Zhang^a, Qingmin Liao^a, Shaojun Liu^b, Haoyu Ma^a, Wenming Yang^a and Jing-hao Xue^{c,1}

^aDepartment of electronic engineering, Tsinghua University

^bDepartment of Electrical and Computer Engineering, The Hong Kong University of Science and Technology

^cDepartment of Statistical Science, University College London

ARTICLE INFO

Keywords:
image fusion
multi-focus
multi-focus dataset
deep learning

ABSTRACT

Multi-focus image fusion, a technique to generate an all-in-focus image from two or more source images, can benefit many computer vision tasks. However, currently there is no large and realistic dataset to perform convincing evaluation and comparison for exiting multi-focus image fusion. For deep learning methods, it is difficult to train a network without a suitable dataset. In this paper, we introduce a large and realistic multi-focus dataset containing 800 pairs of source images with the corresponding ground truth images. The dataset is generated using a light field camera, consequently, the source images as well as the ground truth images are realistic. Moreover, the dataset contains a variety of scenes, including buildings, plants, humans, shopping malls, squares and so on, to serve as a well-founded benchmark for multi-focus image fusion tasks. For illustration, we evaluate 10 typical multi-focus algorithms on this dataset.

1. Introduction

For most computer vision tasks such as object detection and identification, it is clearly desirable to use an in-focus image as input rather than a blurred one. However, due to the limited depth-of-field (DOF) of cameras, it is usually difficult to capture an all-in-focus image directly. Therefore, multi-focus image fusion, a technique to fuse two or more images into an all-in-focus image, is very important in the field of computer vision and image processing, and has drawn much attention in recent years.

Existing multi-focus image fusion methods can be roughly categorized into three groups: transform domain-based methods, spatial domain-based methods, and deep learning-based methods.

Transform domain-based methods usually first decompose the source images in a transform domain, then fuse features in the transform domain and finally reconstruct the fusing image. Laplacian pyramid (LP) [1], wavelet transform [17] ratio of low-pass pyramid (RP) [20], curvelet transform (CVT), discrete wavelet transform (DWT) [9], dual-tree complex wavelet transform (DTCWT) [8], non-subsampled contourlet transform (NSCT) [23], principal component analysis (CPA) [21] and sparse representation-based methods [22, 13, 24] have been proposed.

Spatial domain-based methods can be further classified into three categories: block-based, region-based and pixel-based fusion methods. The block-based methods [5] first divide images into blocks, then calculate the focus measure of each block, and finally choose the block with the highest focus measure as the corresponding block of the fusion result. Consequently, these algorithms are often affected by the accuracy of block partitioning. The region-based methods [10] segment the input of images and then fuse the fo-

cused segments of these input images. Therefore, the fusion results of region-based methods highly rely on the segmentation accuracy. The pixel-based methods [14] calculate the focus measure and fuse the images at pixel level. Unfortunately, pixel-based methods often produce bad results near the focused/defocused boundary.

In the past several years, many deep learning methods has been proposed. Liu *et al.* [12] used a deep convolutional neural network (CNN) to generate a decision map just like pixel-based methods, and then did some post processing to get a final decision map. FuseGan [7] used a generative adversarial network (GAN) to generate decision map. These methods can be taken as network-based implementations of spatial domain-based methods. Different from them, Wen *et al.* [25] designed an end-to-end trained neural network.

One of the bottlenecks of using deep neural networks to solve multi-focus fusion problems is that currently there is no suitable large database with ground truth for the network training. The most widely used dataset is the Lytro Multi-focus Dataset [16], which contains 20 pairs of color multi-focus images of size 520×520 pixels. This dataset is very small and it has no ground-truth, therefore, it is not suitable for training a neural network. To break through this bottleneck, there have been some valuable trials. Liu *et al.* [12] used high-quality natural images blurred by Gaussian filters with five different levels of blur. The data generated by this method was not as real as natural images, because they lack of defocus jump, as the whole image is blurred at the same level. [7, 25] used segmentation datasets which have manually labeled segmentation ground truth. The ground truth were used as a 0-1 mask map, 1 for foreground and 0 for background. Then the images were blurred by Gaussian filters separately and finally merged together. In our previous work BANet[15], we generated a dataset based on an alpha matting dataset. We chose a matted object as a foreground object, and chose a high-quality picture as the


 jinghao.xue@ucl.ac.uk (J. Xue)
ORCID(s):



Figure 1: Example in our dataset. (a) source image focused on the foreground. (b) source image focused on the background. (c) all-in focus image.

Table 1

Comparison of various datasets

Dataset	Data generation method	size	realistic	ground truth
Lytro [16]	Captured by light field camera	20 pairs, 520×520	Yes	No
CNN [12]	Synthetically generated based on the ImageNet dataset	1,000,000 pairs, 16×16	No	Yes
BAnet [15]	Synthetically generated based on the Matting dataset	2268000 pairs, 16×16	No	Yes
FuseGan [7]	Synthetically generated based on segmentation datasets	5850 pairs, 320×480	No	Yes
Our dataset	Captured by light field camera	800pairs, 625×433	Yes	Yes

background. The images generated by these methods do not follow the real defocus model and thus can be improved.

In this letter, we propose a new large and realistic dataset for multi-focus image fusion tasks. The dataset consists of various natural multi-focus images with ground truth, generated by light field images. Figure 1 shows an exemplar pairs of images and ground truth in our dataset. The contributions of our work are twofold.

First, we introduce a new large and realistic multi-focus dataset containing 800 pairs of images that can be used for training deep neural networks. Each pair includes two differently focused images as the source images and a fused image as ground truth. The dataset is generated using a light field camera: Lytro illum camera. The source images are produced by choosing different focus planes.

Secondly, up to present, there is no large and reliable dataset to validate various multi-focus image fusion methods. Our dataset provides a test benchmark for evaluating the multi-focus image fusion algorithms.

2. Related Work

2.1. Multi-focus image fusion dataset

As mentioned above, currently the most widely used multi-focus image fusion dataset [16] only has 20 pairs of images and these images do not have ground truth and thus cannot be used for supervised training of deep neural networks. Therefore, many deep learning-based algorithms [12, 25, 7, 15] generated datasets artificially as the training set. But all of these datasets are not natural or realistic, especially near the focused/defocused boundary. The differences of these datasets are summarized in Table 1.

2.2. Light field image processing

Different from the conventional cameras, the light field camera records the entire light field information on one shooting, and generates images afterwards. In 2005, Ren Ng proposed a Fourier Slice Photography Theorem [19], which proved that images focused at different depths can be computed from a single light field. Dansereau *et al.* [4] designed a 4D hyperfan shaped band-pass filter in the frequency domain which can control the range of focused depths of image in spatial domain.

3. Dataset

3.1. Image capture and categories

We used the Lytro illum camera to capture light field images at different places, such as square, campus, shopping mall and street. Photo categories include people, plants, buildings, objects, etc. In addition to the photos we took ourselves, we also selected 400 images from the Stanford database [2]. We finally selected 800 images as the material of our dataset.

3.2. Refocusing

The main processing of the dataset is refocusing. According to the Fourier Slice Photography Theorem, 4D light field data was first transformed to 4D Fourier spectrum.

$$F(\Omega_u, \Omega_s, \Omega_v, \Omega_t) = DFT(f(u, s, v, t)), \quad (1)$$

where DFT means discrete Fourier transform, f means 4D light field image, F means 4D Fourier spectrum, and u, s, v, t are the two-plane parameterizations of light rays. Then we used 4D hyperfan as a high-dimensional passband filter to

filter the 4D Fourier spectrum .

$$F_{depth} = H_{HF}(\Omega_u, \Omega_s, \Omega_v, \Omega_t, \theta_1, \theta_2)F(\Omega_u, \Omega_s, \Omega_v, \Omega_t), \quad (2)$$

where H_{HF} means 4D hyperfan passband filter, F_{depth} means the Fourier spectrum of 2D image focused on the specific depth, and the parameter θ_1 and θ_2 are the slope parameter of the 4D hyperfan. Finally, the 2D image can be generated by inverse Fourier transform of the processed 4D Fourier spectrum.

$$I = IDFT(F_{depth}), \quad (3)$$

where $IDFT$ means inverse discrete Fourier transform, I means the 2D image focused on the specific depth. According to the specific situation of each picture, the specific depth range of the focus is manually selected in Lytro software. Record the depth of focus of each image, and then use the methods to generate the desired image focused on different depth ranges. The details of the algorithm are shown in Algorithm 1.

Algorithm 1 Refocusing Method

```

for each light field image  $i$  do
  Decode the light field data:  $f$ ;
   $F = DFT(f)$ : Transform  $f$  into the frequency domain
  by FFT;
   $j$  = The depth at foreground;
   $k$  = The depth at background;
   $l = (j + k)/2$ ;
  # Generate the foreground focused image;
   $H_{FG} = H_{HF}(j, l)$ : Build the 4D frequency hyperfan
  with slope  $j$  and  $l$ ;
   $F_{FG} = H_{FG}F$ ;
   $I_{FG} = IDFT(F_{FG})$ ;
  # Generate the background focused image;
   $H_{BG} = H_{HF}(k, l)$ : Build the 4D frequency hyperfan
  with slope  $k$  and  $l$ ;
   $F_{BG} = H_{BG}F$ ;
   $I_{BG} = IDFT(F_{BG})$ ;
  # Generate the all-in-focus image;
   $H_{AF} = H_{HF}(j, k)$ : Build the 4D frequency hyperfan
  with slope  $j$  and  $k$ ;
   $F_{AF} = H_{AF}F$ ;
   $I_{AF} = IDFT(F_{AF})$ ;
end for

```

3.3. Post-processing

From the light field data, we can obtain a raw 2D lenselet image. A raw lenselet image is shown in Figure 2. We used light field toolbox(LFtoolbox) [3] created by Donald G. Dansereau to decode light field data.

But the 2D images generated by LFtoolbox have color deviation and shape distortion. We fixed the color difference problem through the gamma transform, and by using a calibration plate, the problem of shape distortion is solved.

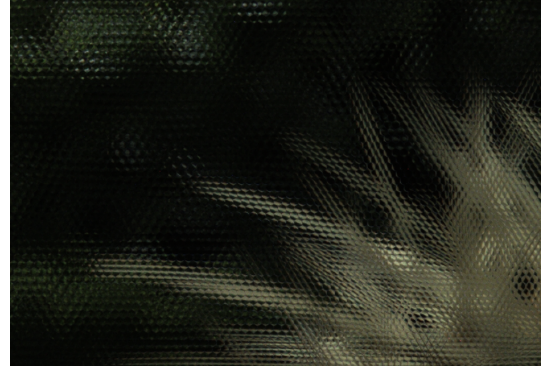


Figure 2: 2D lenselet image.

As shown in Figure 3, the image before color correction is dim and lacks color details. It can be seen that the shape of Figure 3(a) and (b) has obvious distortions, and the table is curved. After shape distortion, the table becomes straight.

4. Experiments

4.1. Dataset

Our dataset contains 800 pairs of images, where each pair includes two source images focused on the foreground and background, respectively, and a fused image as the ground truth. Totally there are 2400 images in our dataset. Figure 4 shows the difference maps between the all-in-focus image and the two source images. We hope that the ground-truth is similar to the composition of two source images: the foreground regions should be similar to the source image focused on the foreground, and the background regions should be similar to the source image focused on the background. Figure 4(d) shows that our ground truth (Figure 4(a)) matches the background of the image focused on the background (Figure 4(b)), and quite different from the foreground(Figure 4(c)). Similar phenomenon can be observed for the background-focused image.

Furthermore, in order to better evaluate the effect of the algorithm on different difficulties, especially for simple and complex boundaries, we manually divide the data set into simple data set (315 pairs) and complex data set (485 pairs) according to the complexity of focused/defocused boundary.

4.2. TestBench

We evaluate tested 10 typical multi-focus image fusion methods, including LP [1], RP [20], DWT [9], CVT [18], DTCWT [8], NSCT [23], SR [22], GF [11], Dsift [14], NSCT-SR [13], CNN [12] on our dataset.

We employed peak signal to noise ratio (PSNR), structure similarity (SSIM) and end point error (EPE) as the evaluation indexes, and the results on the whole dataset are listed in Table 2. We also conducted the test on our simple-dataset and hard-dataset, where the results are shown in Table 3 and Table 4. Unsurprisingly, the results of various algorithms on the simple-dataset are generally better than the corresponding results on the hard-dataset. And the performance of var-

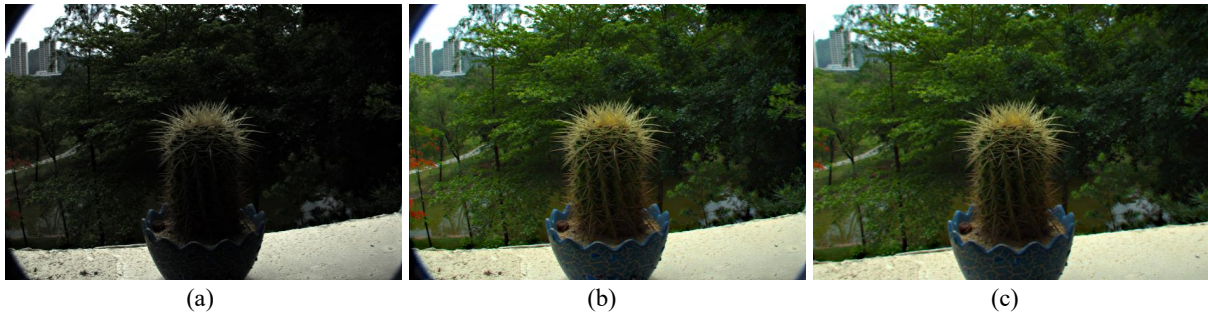


Figure 3: (a) before post-processing. (b) after color correction. (c) after color correction and distortion correction.

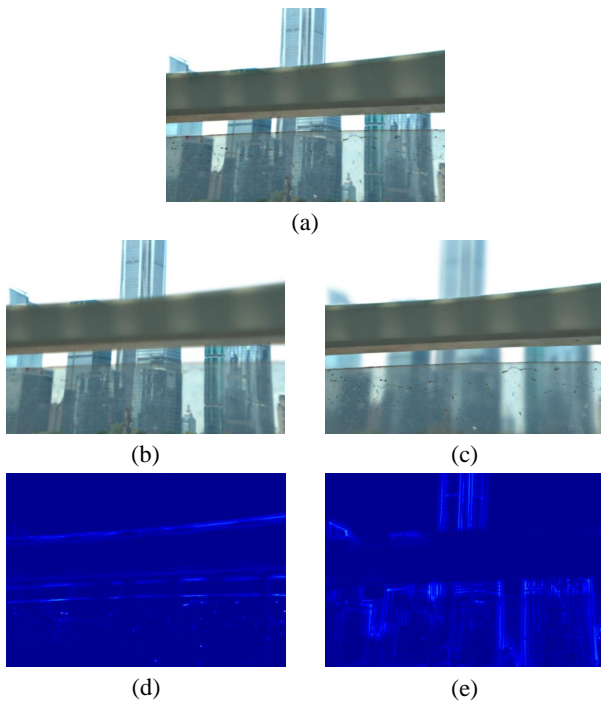


Figure 4: Example in our dataset, (a) is an all-in focus image, (b) is a image focused on the background, (c) is a image focused on the foreground, (d) is the difference map between (a) and (b), (e) is the difference map between (a) and (c).

ious algorithms are similar to those in Table 2. For illustration, we choose an example with complex foreground borders in our dataset, the visual results of various methods are shown in Figure 7. We can see the difference among these ten methods for the regions of the falling leaves and people in the background. It is hard for spatial domain-based methods to generate precise decision map which means the fused image has totally blurry areas. For transform domain-based methods, complex boundaries will decrease the performance of the algorithm, but fortunately this effect will not lead to complete failure for the algorithm. We can see that CNN has blurred results in the falling leaves, and Dsift has blurred results in the people, while NSCT-SR has better results in the both areas.

In order to further analyze whether the difference be-

PSNR	Dsift	CNN	SR	GF	LP	RP	DTC WT	CVT	NSCT	NSCT -SR
Dsift	0	0	0	0	0	0	0	0	0	0
CNN	1	0	1	0	0	1	0	0	0	0
SR	0	0	0	0	0	0	0	0	0	0
GF	1	1	1	0	0	1	0	0	0	0
LP	1	1	1	1	0	1	1	1	1	0
RP	1	0	0	0	0	0	0	0	0	0
DTC WT	1	1	1	1	0	1	0	0	0	0
CVT	1	1	1	0	0	1	1	0	0	0
NSCT	1	1	1	1	0	1	1	1	0	0
NSCT -SR	1	1	1	1	1	1	1	1	1	0

Figure 5: Signification of PSNR. The number '1' indicates that the algorithm of the row is significantly better than the algorithm of the column, and the number '0' indicates that the algorithm of the row is worse than the algorithm of the column, or it is better but not significantly.

SSIM	Dsift	CNN	SR	GF	LP	RP	DTC WT	CVT	NSCT	NSCT -SR
Dsift	0	0	0	0	0	0	0	0	0	0
CNN	1	0	1	0	0	0	0	0	0	0
SR	0	0	0	0	0	0	0	0	0	0
GF	1	1	1	0	0	1	0	0	0	0
LP	1	1	1	1	0	1	1	1	0	0
RP	1	0	1	0	0	0	0	0	0	0
DTC WT	1	1	1	1	0	1	0	1	0	0
CVT	1	1	1	0	0	1	0	0	0	0
NSCT	1	1	1	1	1	1	1	1	0	0
NSCT -SR	1	1	1	1	1	1	1	1	1	0

Figure 6: Signification of SSIM

tween the experimental results of these method is significant, we performed a Friedman test [6] on the experimental results in Table 2. The signification on PSNR and SSIM are shown in Figure 5 and Figure 6. The number '1' indicates that the algorithm of the row is significantly better than the algorithm of the column, and the number '0' indicates that the algorithm of the row is not significantly better than the

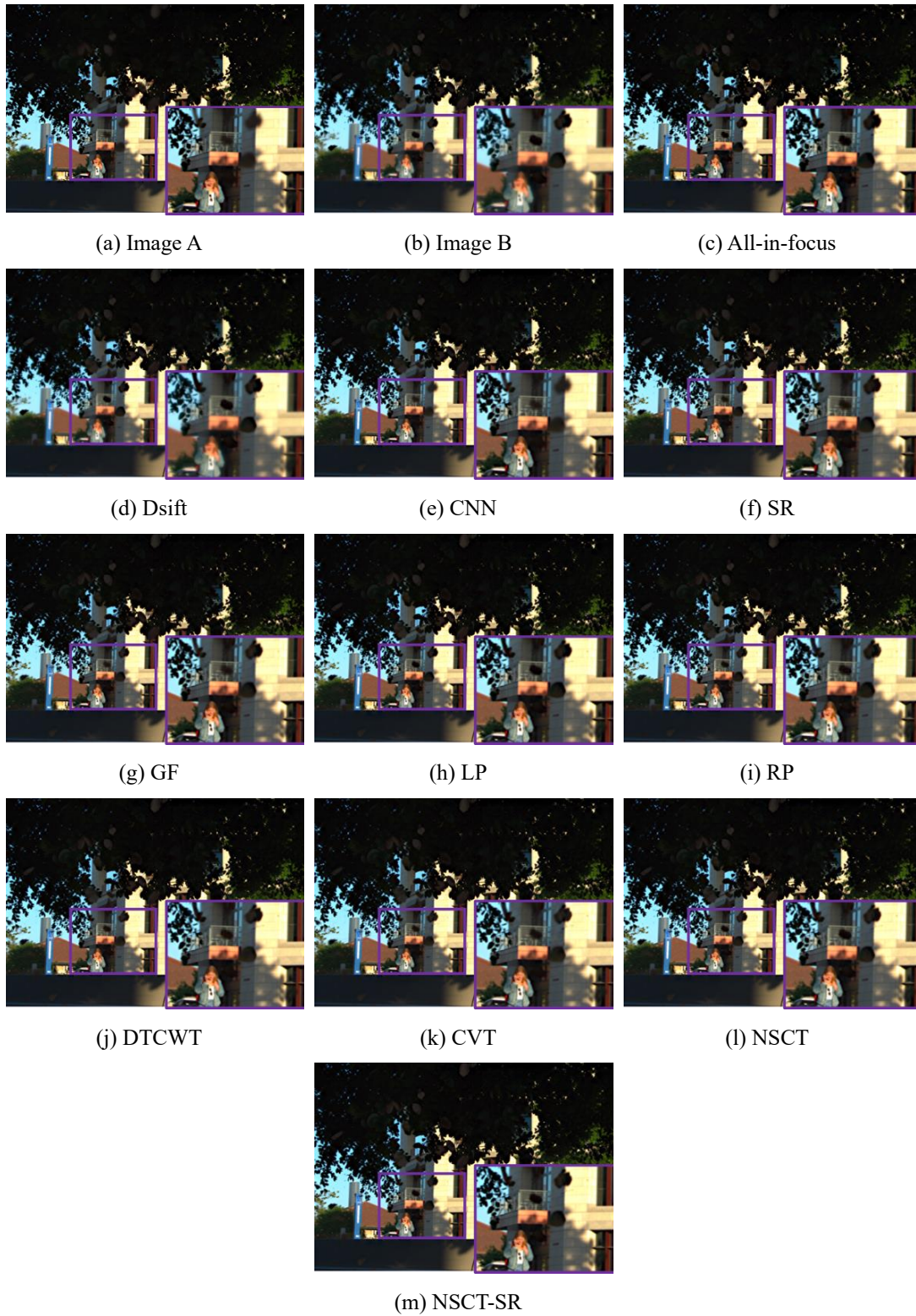


Figure 7: Results.

algorithm of the column. Based on the results, we can say that NSCT-SR is the best performing algorithm in our test.

5. Conclusions

In this paper, we propose a large and realistic dataset for the multi-focus image fusion task. To the best of our knowledge, this is the first large and realistic dataset. The dataset

Table 2

The results of methods on our dataset.

methods	Dsift	CNN	SR	GF	LP	RP	DTCWT	CVT	NSCT	NSCT-SR
PSNR	41.64	41.76	41.53	42.14	42.55	41.7	42.11	42.22	42.5	42.67
SSIM	0.9909	0.9912	0.9911	0.992	0.9929	0.992	0.9921	0.9919	0.993	0.9931
EPE	1.596	1.583	1.636	1.556	1.544	1.664	1.617	1.620	1.514	1.485

Table 3

The results of methods on our simple-dataset.

methods	Dsift	CNN	SR	GF	LP	RP	DTCWT	CVT	NSCT	NSCT-SR
PSNR	46.13	46.7	45.93	46.75	47.12	46.18	46.83	46.89	47.06	47.21
SSIM	0.9947	0.9953	0.9945	0.9954	0.9954	0.9949	0.9953	0.9953	0.9956	0.9957
EPE	0.942	0.905	0.958	0.895	0.881	0.954	0.908	0.907	0.853	0.835

is generated using the light field images captured with a light field camera. We use 4D hyperfan in the frequency domain as a band-pass filter to produce images focused on different depths in our control. We divide it into two sub datasets, simple dataset and complex dataset. The proposed dataset can serve as a test bench for existing multi-focus image fusion methods. Hopefully, it can also benefit the development of deep learning based methods in the future.

6. Acknowledgement

This work was supported by the National Natural Science Foundation of China (61771276).

References

- [1] Burt, P.J., Adelson, E.H., 1983. The laplacian pyramid as a compact image code. *Ieee Transactions on Communications* 31, 532–540. URL: <GotoISI>://WOS:A1983QQ06400008.
- [2] Dansereau, D.G., Girod, B., Wetzstein, G., 2019. LiFF: Light field features in scale and depth, in: *Computer Vision and Pattern Recognition (CVPR)*, IEEE. URL: <http://dgd.vision/Papers/dansereau2019liff.pdf>.
- [3] Dansereau, D.G., Pizarro, O., Williams, S.B., . Decoding, calibration and rectification for lenselet-based plenoptic cameras, in: *CVPR*, pp. 1027–1034.
- [4] Dansereau, D.G., Pizarro, O., Williams, S.B., 2015. Linear volumetric focus for light field cameras. *Acm Transactions on Graphics* 34, 1–20.
- [5] De, I., Chanda, B., 2013. Multi-focus image fusion using a morphology-based focus measure in a quad-tree structure. *Information Fusion* 14, 136–146. URL: <GotoISI>://WOS:000314671900003.
- [6] Friedman, M., 1940. A comparison of alternative tests of significance for the problem of m rankings. *Annals of Mathematical Statistics* 11, 86–92. URL: <GotoISI>://WOS:000188517200006, doi:DOI10.1214/aoms/1177731944.
- [7] Guo, X.P., Nie, R.C., Cao, J.D., Zhou, D.M., Mei, L.Y., He, K.J., 2019. Fusegan: Learning to fuse multi-focus image via conditional generative adversarial network. *Ieee Transactions on Multimedia* 21, 1982–1996. URL: <GotoISI>://WOS:000476809700008, doi:10.1109/Tmm.2019.2895292.
- [8] Lewis, J.J., O’Callaghan, R.J., Nikolov, S.G., Bull, D.R., Canagarajah, N., 2007. Pixel- and region-based image fusion with complex wavelets. *Information Fusion* 8, 119–130. URL: <GotoISI>://WOS:000244574600003.
- [9] Li, H., Manjunath, B.S., Mitra, S.K., 1995. Multisensor image fusion using the wavelet transform. *Graphical Models and Image Processing* 57, 235–245. URL: <GotoISI>://WOS:A1995RB04000005, doi:DOI10.1006/gmip.1995.1022.
- [10] Li, M., Cai, W., Tan, Z., 2006. A region-based multi-sensor image fusion scheme using pulse-coupled neural network. *Pattern Recognition Letters* 27, 1948–1956. URL: <GotoISI>://WOS:000241718600009.
- [11] Li, S.T., Kang, X.D., Hu, J.W., 2013. Image fusion with guided filtering. *Ieee Transactions on Image Processing* 22, 2864–2875. URL: <GotoISI>://WOS:000321924600028.
- [12] Liu, Y., Chen, X., Peng, H., Wang, Z.F., 2017. Multi-focus image fusion with a deep convolutional neural network. *Information Fusion* 36, 191–207. URL: <GotoISI>://WOS:000394070100015.
- [13] Liu, Y., Liu, S.P., Wang, Z.F., 2015a. A general framework for image fusion based on multi-scale transform and sparse representation. *Information Fusion* 24, 147–164. URL: <GotoISI>://WOS:000349736700012.
- [14] Liu, Y., Liu, S.P., Wang, Z.F., 2015b. Multi-focus image fusion with dense sift. *Information Fusion* 23, 139–155. URL: <GotoISI>://WOS:000345181400013.
- [15] Ma, H., Zhang, J., Liu, S., Liao, Q., 2019. Boundary aware multi-focus image fusion using deep neural network, in: *2019 IEEE International Conference on Multimedia and Expo (ICME)*, pp. 1150–1155. doi:10.1109/ICME.2019.00201.
- [16] Nejati, M., Samavi, S., Shirani, S., 2015. Multi-focus image fusion using dictionary-based sparse representation. *Information Fusion* 25, 72–84. URL: <GotoISI>://WOS:000351972800007.
- [17] Nencini, F., Garzelli, A., Baronti, S., Alparone, L., 2007a. Remote sensing image fusion using the curvelet transform. *Information Fu-*

Table 4

The results of methods on our hard-dataset.

methods	Dsift	CNN	SR	GF	LP	RP	DTCWT	CVT	NSCT	NSCT-SR
PSNR	40.98	41.17	41.03	41.59	42.01	40.98	41.58	41.6	41.96	42.17
SSIM	0.9904	0.9909	0.9905	0.9917	0.9925	0.9914	0.9918	0.9915	0.9927	0.9928
EPE	1.693	1.672	1.742	1.639	1.629	1.780	1.708	1.721	1.599	1.556

- sion 8, 143–156. URL: <GotoISI>://WOS:000244574600005.
- [18] Nencini, F., Garzelli, A., Baronti, S., Alparone, L., 2007b. Remote sensing image fusion using the curvelet transform. *Information Fusion* 8, 143–156. URL: <GotoISI>://WOS:000244574600005.
- [19] Ng, R., 2005. Fourier slice photography. *Acm Transactions on Graphics* 24, 735–744. URL: <GotoISI>://WOS:000231223700044.
- [20] Toet, A., 1989. Image fusion by a ratio of low-pass pyramid. *Pattern Recognition Letters* 9, 245–253. URL: <GotoISI>://WOS:A1989U956600003, doi:Doi10.1016/0167-8655(89)90003-2.
- [21] Wan, T., Zhu, C.C., Qin, Z.C., 2013. Multifocus image fusion based on robust principal component analysis. *Pattern Recognition Letters* 34, 1001–1008. URL: <GotoISI>://WOS:000318889800007.
- [22] Yang, B., Li, S.T., 2010. Multifocus image fusion and restoration with sparse representation. *Ieee Transactions on Instrumentation and Measurement* 59, 884–892. URL: <GotoISI>://WOS:000275368500016.
- [23] Zhang, Q., Guo, B.L., 2009. Multifocus image fusion using the non-subsampled contourlet transform. *Signal Processing* 89, 1334–1346. URL: <GotoISI>://WOS:000265508200006.
- [24] Zhang, Q., Shi, T., Wang, F., Blum, R.S., Han, J.G., 2018. Robust sparse representation based multi-focus image fusion with dictionary construction and local spatial consistency. *Pattern Recognition* 83, 299–313. URL: <GotoISI>://WOS:000442172200023.
- [25] Zhao, W.D., Wang, D., Lu, H.C., 2019. Multi-focus image fusion with a natural enhancement via a joint multi-level deeply supervised convolutional neural network. *Ieee Transactions on Circuits and Systems for Video Technology* 29, 1102–1115. URL: <GotoISI>://WOS:000464149700015, doi:10.1109/Tcsvt.2018.2821177.